PHYSICAL REVIEW ACCELERATORS AND BEAMS **25,** 083401 (2022)

Slice energy spread measurement in the low energy photoinjector

Houjun Qian,* Mikhail Krasilnikov,† Anusorn Lueangaramwong, Xiangkun Li,
Osip Lishilin, Zakaria Aboulbanine, Gowri Adhikari, Namra Aftab,
Prach Boonpornprasert, Georgi Georgiev, James Good, Matthias Gross,
Christian Koschitzki, Raffael Niemczyk, Anne Oppelt, Guan Shu, Frank Stephan,
Grygorii Vashchenko, and Tobias Weilbach

Deutsches Elektronen-Synchrotron DESY, Platanenallee 6, 15738 Zeuthen, Germany

(Received 28 January 2022; accepted 6 July 2022; published 8 August 2022)

Slice energy spread is one of the key parameters in free electron laser optimizations, but its accurate measurement is not straightforward. Two recent studies from high energy (≥ 100 MeV) photoinjectors at SwissFEL and European x-ray free electron laser (XFEL) have reported much higher slice energy spread than expected at their XFEL working points (200–250 pC). In this paper, a new method for measuring slice energy spread at lower beam energy (~20 MeV) is proposed and demonstrated at the PhotoInjector Test facility at DESY Zeuthen, and the results for 250 pC are much lower than those measured at high energy injectors.

DOI: 10.1103/PhysRevAccelBeams.25.083401

I. INTRODUCTION

High brightness electron beams are critical for many scientific instruments, such as electron microscopes and x-ray free electron lasers (XFELs), which have transformed modern research with unprecedented spatial, temporal, and energy resolutions [1–4]. Beam brightness scales as beam density in the six-dimensional (6D) phase space

$$B_{6D} \propto \frac{\partial^3 Q}{\partial \varepsilon_{nx} \partial \varepsilon_{ny} \partial \varepsilon_{nz}} \propto \frac{I/\sigma_E}{\varepsilon_{nx}\varepsilon_{ny}}, \tag{1}$$

where Q is the bunch charge, I is the peak current, σ_E is the uncorrelated energy spread or slice energy spread, ε_{nx}, ε_{ny}, and ε_{nz} are normalized emittances. While the beam brightness directly measures the performance of electron microscopes, it indirectly determines the XFEL brilliance by affecting the amplification gain in the undulator [5,6]. Therefore, the measurement of 6D beam brightness is an indispensable part of XFEL optimizations. For linac based XFELs, beam brightness optimization has to start from the injector due to Liouville's theorem. Both transverse emittance and beam peak current can be routinely measured in an XFEL injector, but accurate slice energy spread measurement is still not trivial. This is because photoinjector slice energy spread is expected to be on the 1 keV level, which is below the measurement resolution of standard procedures [7]. In the past, accurate slice energy spread measurement for XFEL injector was not that critical, because it is much lower than required and even causes microbunching instability to reduce XFEL lasing [8–12]. Therefore, a laser heater is used to increase the injector slice energy spread to damp such instability to improve FEL lasing [13–15]. With the improvement of electron source brightness and undulator technology, compact XFEL machines or continuous wave (cw) XFEL machines of lower beam energy were built or under development, such as SACLA, SwissFEL, LCLS-II, European XFEL, and SHINE [6,16–21]. An efficient FEL amplification requires the following conditions:

$$\frac{\varepsilon_{\mathrm{n}}}{\gamma} < \frac{\lambda}{4\pi}, \tag{2}$$

$$\frac{\sigma_\gamma}{\gamma} < \rho, \tag{3}$$

where γ is the beam Lorentz factor, λ is the FEL radiation wavelength, ε_{n} is the normalized emittance, σ_γ is the normalized slice energy spread, and ρ is the FEL Pierce parameter [5]. With lower linac energy, the requirements on both transverse and longitudinal beam brightness get tighter for lasing at the shortest wavelength. Ultrahigh gradient pulsed guns are under development to achieve both low emittance and high peak current in the pancake photoemission regime [6,22–26], while cw guns try to improve transverse emittance in the cigar photoemission

---

*houjun.qian@desy.de

†mikhail.krasilnikov@desy.de

TABLE I. Summary of slice energy spread measurements.

	SDUV	FERMI	SwissFEL	Eu-XFEL	Unit
Q	100	600	200	250	pC
E_k	136	1320	100	130	MeV
I	12	800	20	20	A
σ_E	1.2	40	15	5.9	keV
I/σ_E	10	20	1.3	3.4	A/keV
Method	Undulator radiation		Dispersion		…
Reference	[33]	[40]	[31]	[32]	…

regime with a lower peak current [27–30]. Besides, the threshold for injector slice energy spread also gets lower due to the lower linac energy.

Recently, two dispersion based methods were proposed and demonstrated for accurate injector slice energy spread measurements with rms uncertainty down to the 0.1 to 0.3 keV level [31,32]. Both measured much higher slice energy spread than expected for 200 to 250 pC bunch charge, which reduced the laser heater's role in improving XFEL lasing. Alternatively, the slice energy spread can be reconstructed based on undulator radiation. Here one can measure the radiation dependence on the longitudinal dispersion strength either in a high-gain harmonic generation scheme [33] or in an optical klystron configuration [34,35]. Compared to self-amplified spontaneous emission XFEL, seeded XFEL prefers an even lower slice energy spread for high harmonic generation [36–39]. A summary of high resolution slice energy spread measurements is shown in Table I, and the two hard x-ray injectors show much lower longitudinal beam brightness than the two seeded FEL injectors.

In this paper, we introduce a dispersion based method to measure the slice energy spread at the low energy (20 MeV) PhotoInjector Test facility at DESY Zeuthen (PITZ). In addition to the low beam energy, tungsten slit masks are used to reduce the beam transverse emittance, therefore energy spread measurement resolution improves compared to a high energy injector. The paper is organized as follows: First, the methodology is described in Sec. II. Then, the experiments for 250 pC are presented in Sec. III. Finally, a discussion and summary are given in Secs. IV and V.

II. METHODOLOGY

Slice energy spread is usually measured with an rf transverse deflecting structure (TDS) and a dipole magnet, which maps the longitudinal phase space (LPS) of the beam to the transverse distribution on a screen in a dispersion section. As was discussed in [31], the beam size along the energy dispersion direction consists of four contributions, i.e., screen spatial resolution, transverse emittance effect, TDS-induced energy spread, and true slice energy spread. The convolution of the four contributions can be expressed as

$$\sigma_{\mathrm{total}}^2 = \sigma_{\mathrm{scr}}^2 + \frac{\varepsilon_{\mathrm{n1}}\beta_{\mathrm{scr}}}{\gamma} + \left(D\frac{\sigma_\gamma}{\gamma}\right)^2 + \left(D\frac{\sigma_{\gamma,\mathrm{TDS}}}{\gamma}\right)^2, \quad (4)$$

where σ_{total} is the total rms beam size, σ_{scr} is the rms screen resolution, $\varepsilon_{\mathrm{n1}}$ is the normalized slice emittance in the dipole bending plane, β_{scr} is the beta function at measurement screen, D is the dispersion function, and $\sigma_{\gamma,\mathrm{TDS}}$ is the slice energy spread due to the transverse acceleration gradient in TDS.

The energy spread $\sigma_{\gamma,\mathrm{TDS}}$ depends linearly on the TDS deflection voltage, therefore it can be extracted by a TDS voltage scan. After removing the TDS contribution, there are two methods to extract the net slice energy spread σ_γ from the other contributions. The first is demonstrated at the SwissFEL by scanning the beam energy γ [31]. The second is demonstrated at the European XFEL by scanning the dispersion function D [32]. Both methods require a constant slice emittance and constant beta function at the measurement screen, which is not easy to achieve for a space charge dominated low energy photoinjector like PITZ.

A. Energy spread resolutions: Low energy versus high energy

The photoinjector slice energy spread is very low in free electron laser applications, expected to be few keV from simulations [41]. To reduce the measurement error of σ_γ, the contributions from the other three terms in Eq. (4) cannot be much larger than σ_γ, otherwise, it puts a tight requirement on machine stability and other measurement errors. Therefore, contributions from screen resolution, transverse emittance, and TDS should be as low as possible. The energy spread resolution due to screen resolution and transverse emittance can be expressed as

$$\sigma_{\gamma,\mathrm{scr}} = \frac{\sigma_{\mathrm{scr}}}{D}\gamma, \quad (5)$$

$$\sigma_{\gamma,\varepsilon} = \frac{\sqrt{\varepsilon_{\mathrm{n1}}\beta_{\mathrm{scr}}}}{D}\gamma^{\frac{1}{2}}. \quad (6)$$

The best energy and time resolutions by TDS in the linear approximation are [42,43]

$$\sigma_{\gamma,\mathrm{TDS}} = \frac{ek_{\mathrm{TDS}}V_{\mathrm{TDS}}}{m_0c^2}\sqrt{\frac{\varepsilon_{\mathrm{n2}}\beta_{\mathrm{TDS}}}{\gamma}}, \quad (7)$$

$$\sigma_t = \frac{m_0c}{ek_{\mathrm{TDS}}V_{\mathrm{TDS}}\sin(\psi)}\sqrt{\frac{\varepsilon_{\mathrm{n2}}\gamma}{\beta_{\mathrm{TDS}}}}, \quad (8)$$

$$\sigma_t\sigma_{\gamma,\mathrm{TDS}} = \frac{\varepsilon_{\mathrm{n2}}}{c\,\sin(\psi)}, \quad (9)$$

where e is elementary charge, c is speed of light, $\varepsilon_{\mathrm{n2}}$ is the normalized slice emittance in the TDS streaking plane, β_{TDS} is the beam beta function in the TDS, k_{TDS} is the TDS wavenumber, V_{TDS} is the TDS transverse voltage, and ψ is the phase advance between TDS and the LPS measurement screen.

In case of the same σ_{scr}, D, ε_{n}, β_{scr}, Eqs. (5) and (6) show that better absolute energy spread resolution can be achieved with lower beam energy. For LPS measurements, its best time and energy resolution product is limited by the transverse emittance and phase advance only. A better time resolution from TDS will lead to a worse energy spread resolution for the LPS measurement.

Taking the parameters from the European XFEL injector as an example [32], beam energy is 130 MeV, dipole screen resolution is 28 μm with an energy dispersion of 1.2 m, and nominal emittance is 0.4 μm for 250 pC [32,44]. The screen-induced energy spread resolution is 3 keV, but it can be reduced to 0.5 keV if the beam energy is lowered to 20 MeV. The product of TDS time resolution and energy resolution is at least 0.68 keV ps based on Eq. (9). If the temporal resolution of TDS measurement reaches a 1 ps (FWHM), i.e., 0.42 ps rms, TDS will induce an rms energy spread of at least 1.6 keV.

B. TDS voltage scan

Since $\sigma_{\gamma,\mathrm{TDS}}$ is linearly proportional to V_{TDS} when the beam size in TDS is fixed, Eq. (4) can be rewritten as

$$\sigma_{\mathrm{total}}^2 = \sigma_0^2 + \left(\sigma_1 \frac{V_{\mathrm{TDS}}}{V_1}\right)^2, \qquad (10)$$

where σ_0^2 is the sum of the first three terms on the right-hand side of Eq. (4), which are independent of TDS voltage. During TDS streaking with voltage V_1, the induced energy spread by TDS will contribute to an rms beam size of σ_1 at the dispersion screen. With a scan of σ_{total} versus V_{TDS} in experiment, σ_0 can be fitted.

Let us assume a 3% rms error for σ_{total} measurement. Here a numerical example is used to show the sensitivity of σ_0 fitting error on the TDS voltage scan range. Let us assume the TDS voltage scan has six voltages uniformly distributed between V_1 and V_{max}. For each TDS voltage, σ_{total} is calculated based on Eq. (10), and a random relative error with a 3% rms value is added. With six TDS voltages and corresponding energy spread values, σ_0 can be fitted. Such a process is repeated 1000 times, and the rms relative errors are shown in Fig. 1 for different measurement configurations. The simulations show that the fitting error depends critically on σ_1, i.e., V_1. To keep the fitting error of σ_0 below 10%, σ_1 should be smaller than σ_0. With the TDS voltage scan range V_{max}/V_1 between 1.5 and 3, the fitting error is not sensitive to V_{max}. If the measurement error of σ_{total} is even larger than 3%, then σ_1 should be even smaller to reach the 10% fitting error.

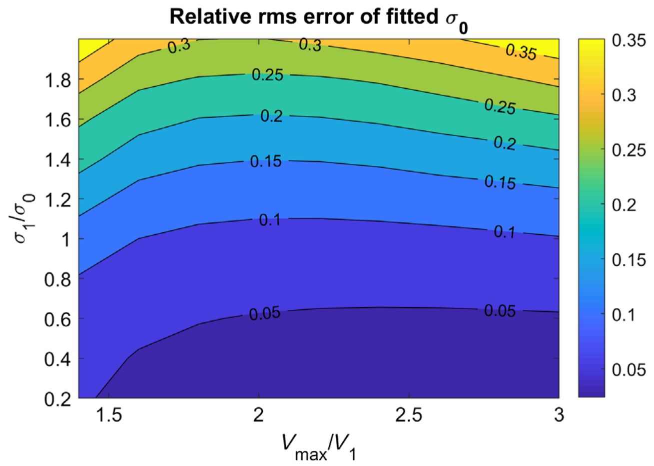

FIG. 1. Relative rms error of σ_0 versus TDS voltage scan configuration.

Based on Eq. (9), a smaller σ_1 means a worse time resolution, which might increase the measurement error of σ_1 by including time correlated energy spread from the acceleration rf curvature. If the rms time resolution of the TDS streaking at the lowest voltage V_1 is σ_{t1}, and the beam energy curvature is simplified to be $E = E_0 \cos(\omega_{rf} \times t)$, then the measured slice energy spread at V_1 will have a contribution from beam energy curvature of $E_0(\omega_{rf}\sigma_{t1})^2/\sqrt{2}$. Assuming a 1 ps rms time resolution for a 20-MeV beam at V_1, the energy curvature contributes an rms energy spread of 0.94 keV. With higher beam energy or linear energy chirp included, this contribution at V_1 is even larger. Since the energy spread from rf curvature due to a limited time resolution is not the real slice energy spread, this term should be reduced compared to the contributions from screen resolution, transverse emittance, and real slice energy spread in Eq. (4), which means the linear energy chirp at the time slice should be minimized, and the time resolution at the minimum TDS voltage should be optimized. Therefore, both good time resolution and low energy spread contribution from TDS at voltage V_1 is preferred, which means a low transverse emittance in the TDS streaking plane is critical according to Eq. (9).

C. Slice energy spread measurement in a low energy beamline

Once the slice energy spread from TDS is precisely removed, slice energy spread σ_γ measurements are limited by screen resolution and transverse emittance effect. Energy scan or dispersion scan methods demonstrated for high energy injectors at SwissFEL and European XFEL [31,32] can not be easily applied to low energy beamlines, where constant slice emittance and beta function are difficult to maintain under the space-charge effect. Instead, we propose to measure the screen resolution and emittance-induced beam size directly. Figure 2 shows the schematic beamline for slice energy spread measurements at PITZ. A 20-MeV high brightness beam is produced by a 1.3-GHz photoinjector and sent to an LPS diagnostic section consisting mainly of an S-band TDS and a dipole magnet [45,46]. The TDS streaks the beam temporally in the vertical direction [47], and the dipole bends the beam horizontally. The energy dispersion function is 0.9 m at the

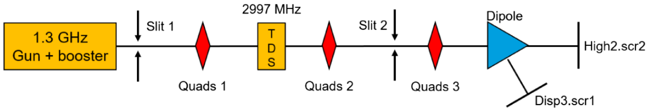

FIG. 2. Schematic beamline for slice energy spread measurement at PITZ (element positions are not in proportion).

LPS measurement screen (Disp3.scr1) [45]. The 1.3-GHz rf gun is the same type of gun as the ones used at FLASH and European XFEL [48–50]. The photoinjector can produce long bunch trains with a micro repetition rate of 1 MHz, but the TDS can only streak up to three pulses in a train due to its short rf pulse length.

There are two slit stations shown in Fig. 2, and both of them have horizontal slits and vertical slits to cut the beam [51]. In this paper, horizontal slit reduces beam vertical emittance, and vertical slit reduces beam horizontal emittance. Slit 1 with a 50 μm opening is used to cut the beam vertical emittance to improve the TDS time and energy resolutions, as indicated by Eq. (9). Quadrupole magnet group 1 tunes the beam size inside the TDS to reduce $\sigma_{y,\mathrm{TDS}}$. Slit station 2 will be used to measure screen resolution and transverse emittance-induced beam size at the LPS measurement screen station Disp3.scr1.

For the Disp3.scr1 resolution measurement, a horizontal slit 2 with 10 μm opening cuts the beam. Since the beam size before slit 2 is much larger than 10 μm, the vertical beam distribution is quasiuniform after slit cut. Therefore, the vertical rms size at the slit exit is 2.9 μm. Due to such a negligible vertical beam size and negligible space-charge effect after the slits, the vertical rms beam size on Disp3.scr1 equals

$$\sigma_y^2 \approx \sigma_{\mathrm{scr,\,D3}}^2 + (R_{12y} \cdot \sigma_{y',\mathrm{slit2}})^2, \tag{11}$$

where R_{12y} is the transfer matrix element from slit 2 to Disp3.scr1, $\sigma_{y',\mathrm{slit2}}$ is the beam divergence after slit 2 cut, and $\sigma_{\mathrm{scr,\,D3}}$ is the screen resolution of Disp3.scr1. The R_{12y} can be either calculated if a reliable lattice model is established or measured directly by orbit response. By scanning R_{12y}, using quadrupole group 3, and measuring vertical rms size on Disp3.scr1, the screen resolution can be fitted based on Eq. (11).

For measuring emittance-induced horizontal beam size on Disp3.scr1, the vertical slit 2 is used, and the horizontal slit 2 is removed. The final slice energy spread is measured with a combination of horizontal slit 1 and vertical slit 2. To allow enough charge for the slice energy spread measurement, the vertical slit 2 opening is 50 μm. After slit 2 cut, the beam horizontal rms size is 14.4 μm, which is much smaller than horizontal beam size on High2.scr2 when dipole magnet is off, and can be neglected. So, the horizontal beam size at High2.scr2 equals

$$\sigma_x^2 \approx \sigma_{\mathrm{scr,\,H2}}^2 + (R_{12x,\mathrm{H2}} \cdot \sigma_{x',\mathrm{slit2}})^2, \tag{12}$$

where $R_{12x,\mathrm{H2}}$ is the transfer matrix element from slit 2 to High2.scr2, $\sigma_{x',\mathrm{slit2}}$ is the beam divergence after slit 2 cut, and $\sigma_{\mathrm{scr,\,H2}}$ is the screen resolution of High2.scr2. Similar to screen resolution measurement, by varying $R_{12x,\mathrm{H2}}$, both screen resolution and beam divergence can be fitted. Then beam emittance-induced beam size at Disp3.scr1 can be calculated as $R_{12x,\mathrm{D3}} \cdot \sigma_{x'\mathrm{slit2}}$, where $R_{12x,\mathrm{D3}}$ is the transfer matrix element from slit 2 to Disp3.scr1.

After slice energy spread contributions from TDS, screen resolution and transverse emittance are measured, the real slice energy spread can be extracted via Eq. (4).

D. Start-to-end simulations of the measurement

In the above proposal, the beam at the dispersion screen is cut by two slits to reduce both vertical emittance and horizontal emittance for a better measurement resolution. Therefore, the measured slice energy spread is actually for the beam after the second slit. If the slice energy spread is uncorrelated before the first slit, i.e., uncorrelated with both transverse and longitudinal coordinates, then the slice energy spread after the second slit should also be close to the slice energy spread before the first slit, because the bunch charge after the first slit cut is low and the space-charge forces and other collective effects are negligible. In the 20-MeV beamline, the beam transverse optics is dominated by the space-charge effect instead of emittance before the first slit. If the slice energy spread is dominated by the space-charge effect instead of the other collective effects, e.g., intrabeam scattering [52,53], microbunching instability [8–12], a correlation between beam energy and transverse coordinates may lead to a slice energy spread reduction after the first slit cut. This will change the correspondence between the measured slice energy spread and the actual slice energy spread of the full beam before the first slit. Therefore, we perform start-to-end simulations to investigate this potential issue.

As shown later, the two slits reduce the bunch charge by a factor of 50. In order to have enough statistics for calculating the slice energy spread after two slit cuts, 2×10^6 macroparticles are used to simulate the full beam before the slits with ASTRA code [54], and 40,000 macroparticles will be left to simulate the beamlet after the slit cut. The transverse distribution of the initial cathode emission is adapted to the measured laser profile on the virtual cathode, which is a 1 mm quasiuniform distribution. The average radial density profile of the cathode laser is considered, but the azimuthal laser nonuniformity is neglected in ASTRA simulations. The laser temporal distribution is assumed to be an ideal Gaussian distribution of 3 ps rms duration. The bunch charge is 250 pC, and the solenoid is set to the optimum emittance compensation to achieve the lowest transverse emittance at the first slit location. Then the beam distribution is further tracked through the slice energy spread measurement beamline in Fig. 2 with OCELOT code [55], including 3D space-charge effects. The simulation

TABLE II. Simulation parameters.

Parameter	Value	Units
Charge	250	pC
Momentum	19.5	MeV/c
Peak current	20	A
100% emittance at first slit	0.6	μm
Slit width	50	μm
TDS frequency	2997	MHz
Dispersion	0.9	m
Screen resolution	70	μm

parameters are listed in Table II according to our measurement beamline.

The 250 pC beam longitudinal phase space distribution right before the first slit is shown in Fig. 3(a). Since the beam is space-charge dominated and rotational symmetric at the first slit, Fig. 3(b) shows a clear correlation between beam energy and radial position in the central temporal slice. The central slice energy spread after the first slit cut versus the slit width is shown in Fig. 4. The first horizontal slit width is 50 μm, and the slice energy spread is reduced from 1.4 keV before the slit to 1.0 keV after the slit. Simulations of the high energy (~130 MeV) injector show such a correlation between slice beam energy and transverse coordinates is diluted through betatron oscillations when the beam becomes emittance dominated.

The slice energy spread from ASTRA simulations is much lower than that measured at European XFEL and SwissFEL injector, which indicates some heating effect is not included in our injector simulations, such as laser temporal profile modulation, intrabeam scattering, or microbunching instability. The intrabeam scattering effect for both European XFEL injector and PITZ injector has been simulated, but the results are still far from measurement values [56]. In order to study the additional heating effect on the measurement procedure, energy spread uncorrelated with both spatial and temporal coordinates is added to the beam right before the first slit numerically, and then the beam is sent to the measurement beamline in OCELOT code to continue start to end simulations of the measurement.

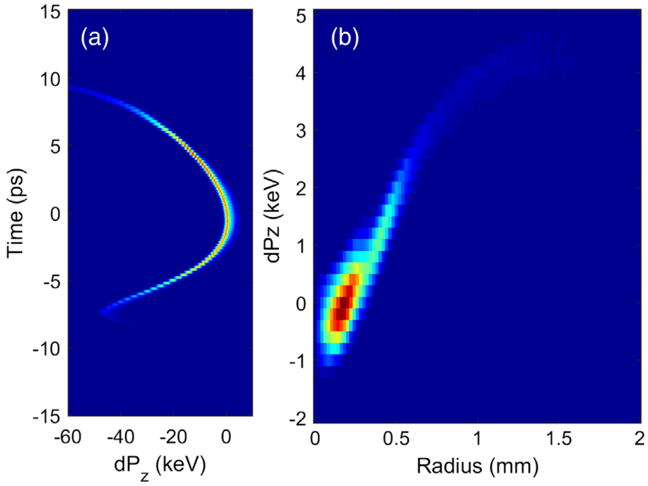

FIG. 3. Beam distribution from ASTRA simulations, right before the first slit. The reference beam momentum is 19.5 MeV/c. (a) Longitudinal phase space. (b) Correlation between beam energy and radial beam position in the central temporal slice (−0.5 ps to 0.5 ps).

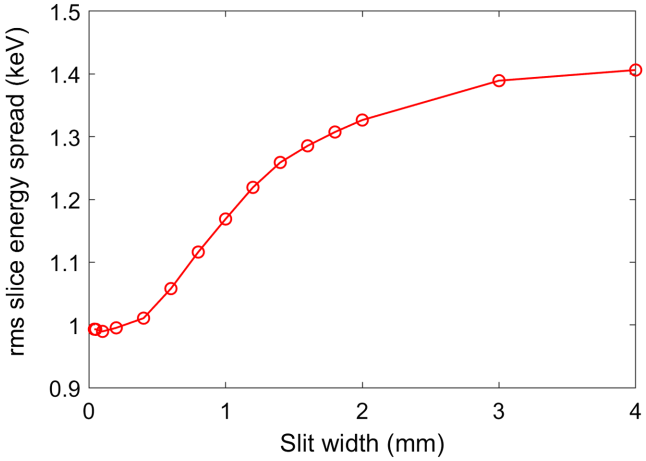

FIG. 4. ASTRA simulations of beam cut by the first slit. Slice energy spread of the central temporal slice (−0.5 ps to 0.5 ps) versus the slit width. The slit width in the experiment is 0.05 mm.

The measurement of slice beam divergence at the second slit exit based on Eq. (12) is simulated and displayed in Fig. 5. The TDS voltage is set to 100 kV, and the R12 between the second slit and the measurement screen is varied with quadrupole group 3. The fitted slice beam divergence multiplied by the R12 between the slit and the dispersion screen Disp3.scr1 approximates the slice emittance contribution in slice energy spread measurement when the beam is cut by the second slit. By setting energy spread to zero at the second slit in OCELOT, the true beam

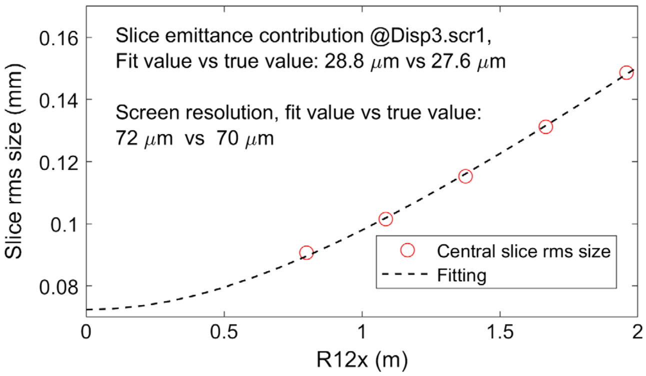

FIG. 5. OCELOT simulation of slice beam size versus R12x scan between slit 2 and High2.scr2. High2.scr2 screen resolution and slice beam divergence contributions are fitted based on Eq. (12). The product of $R_{12x,\mathrm{D3}}$ and slice beam divergence $\sigma_{x',\mathrm{slit2}}$ gives the emittance contribution to beam size at the dispersion screen.

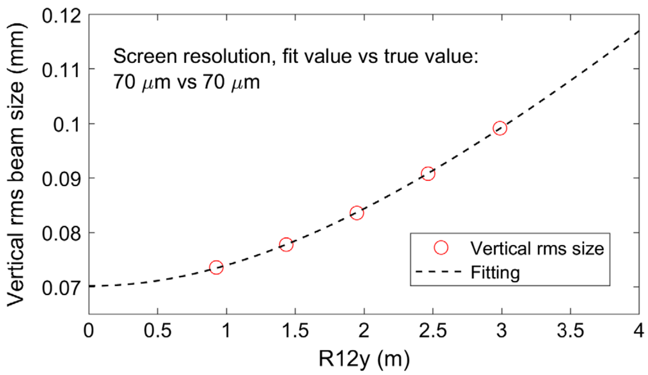

FIG. 6. OCELOT simulation of vertical beam size versus R12y scan between slit 2 and Disp3.scr1. Screen resolution is fitted based on Eq. (11).

size contribution from slice emittance at the dispersion screen is also calculated. As displayed in Fig. 5, the fitted values of the screen resolution (72 μm) and the slice emittance contribution (28.8 μm) are very close to true values. Similarly, the Disp3.scr1 screen resolution measurement is also simulated according to Eq. (11), and the results are displayed in Fig. 6.

The TDS-induced energy spread is extracted by TDS voltage scan based on Eq. (10). Once the contributions of the slice emittance, screen resolution, and TDS-induced energy spread are extracted, the slice energy spread can be calculated. In Fig. 7, the “measured” slice energy spread versus the true slice energy spread at both slits are presented. As expected, simulations show the slit based slice energy spread measurement gives the results for the beam after the second slit cut. When the beam slice energy spread becomes uncorrelated with its spatial coordinates, either through betatron oscillations for emittance dominated beam or due to the nature of the beam heating mechanism, the measured slice energy spread can also be very close to the true slice energy spread of the full beam before the first slit. In that case, the slit cut not only improves the measurement resolution and reduces the collective effects in the measurement process but also keeps the true uncorrelated slice energy spread of the full beam before the first slit cut.

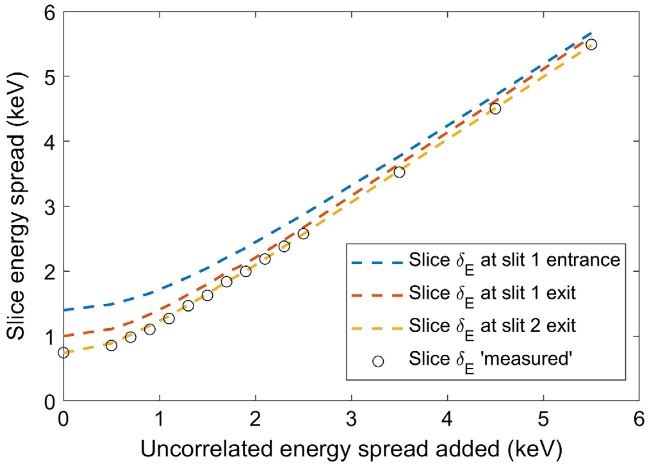

FIG. 7. OCELOT simulation of measured slice energy spread versus true slice energy spread at both slits. The added energy spread at slit 1 entrance is uncorrelated with both spatial and temporal coordinates, and this is to simulate the additional beam heating effect not included in the start-to-end modeling.

III. MEASUREMENTS

As mentioned already, recent slice energy spread measurements at the photoinjectors of SwissFEL and European XFEL have shown slice energy spread much higher than expected from simulations [31,32]. This is either due to high slice energy spread already from the low energy section or due to slice energy spread growth during the high energy acceleration and transportation. This motivated us to measure the slice energy spread in the low energy (20 MeV) injector at PITZ, which has the same rf gun as the European XFEL.

In the experiment, the rf gun and the cathode laser mimic the 250 pC working point of the European XFEL injector [44,57,58]. The photoelectron beam is generated by a UV laser illuminating the $\mathrm{Cs_2Te}$ cathode. Cathode laser diameter is 1 mm with a quasiuniform distribution. Temporally, the laser is 7 ps (FWHM) with a Gaussian distribution. The rf gun accelerates the beam to 6.3 MeV/c with a cathode gradient of 58 MV/m. Then, the beam is matched into the booster linac by solenoid focusing for optimum emittance at the booster exit. Finally, the 20 MeV beam is sent to the diagnostic beamline for slice energy spread measurement. The beam peak current is measured by the TDS to be 20 A.

As discussed in Sec. II C, the high resolution LPS measurement is done with both slit 1 and slit 2. Slit 1 is used to reduce vertical emittance to increase TDS resolution, and slit 2 is used to reduce horizontal emittance-induced energy spread resolution on Disp3.scr1. Both slits have 50 μm opening. In order to measure the low charge beams, 500 μm thick LYSO:Ce is used as screen material at High2.scr2 and Disp3.scr1 [59]. Quadrupole group 1 reduces the vertical beam size in the TDS to lower the TDS-induced energy spread, and quadrupole group 2 optimizes the time resolution of LPS measurement. Quadrupole group 3 varies R_{12y} and R_{12x} for measuring screen resolution and emittance-induced energy resolution, respectively.

The slit 1 effect on vertical beam emittance is shown in Fig. 8. In the optimum emittance compensation working point, the normalized vertical rms emittance is around 0.6 μm. The beam profile without slit 1 cut is measured near quadrupole group 1 when they are off, shown in Fig. 8(a). After the slit 1 insertion, the beam profile is shown in Fig. 8(b). The charge of the reduced beamlet is estimated to be 25 pC, and the vertical rms size is reduced to 0.17 mm. The drift distance from the slit 1 to the beam profile measurement screen is 3.1 m, so the reduced vertical

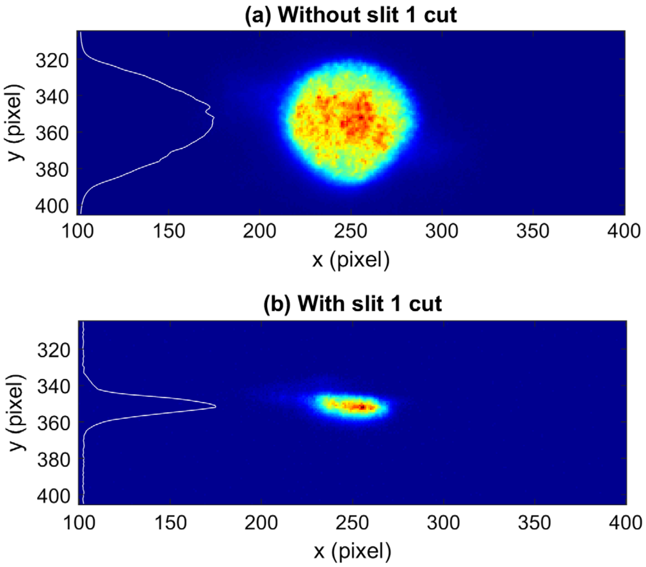

FIG. 8. Beam images measured at 3.1 m downstream slit 1, near quadrupole group 1, when quadrupole group 1 is off, (a) without slit 1 cut, (b) with slit 1 cut. Image calibration is 38.7 μm/pixel.

beam divergence is 55 μrad. Based on the 50 μm slit width and the quasiuniform beam distribution at slit exit, the reduced rms beam size is about 14.4 μm. Considering negligible correlation for the beamlet in the vertical phase space, the normalized vertical emittance is estimated to be 30 nm. This is a factor of 20 reduction compared to the nominal case and improves the LPS resolution significantly.

The TDS voltage scan with and without slit 1 insertion is shown in Fig. 9. The bunch charge after the second slit is about 5 pC, and the LPS image of the 5 pC beam is shown in Fig. 10 for 140 kV TDS streaking. The slice energy spread is calculated for the slice at the TDS zero crossing phase, and the fitted result of 2.3 keV in Fig. 9 still includes contributions from screen resolution and slice emittance. To reduce the correlated energy spread in the slice, the booster linac phase is tuned to minimize linear energy chirp at the TDS zero crossing phase. This is very important for the first TDS voltage, whose time resolution is the worst among all TDS voltages. Figure 9 shows the advantage of small vertical emittance after slit 1 cut. Without slit 1 cut, it is difficult to find both good time resolution and low energy spread. The high energy spread at the first TDS voltage increases the fitting error as shown in Fig. 1. With the slit 1 insertion, a much smaller vertical emittance reduces the product of TDS time and energy resolution significantly. The vertical beam size in the TDS is reduced by quadrupole group 1 to reduce energy spread growth while a good time resolution can still be maintained at Disp3.scr1. The slice energy spread growth by the first TDS voltage is almost negligible, therefore the rms error is reduced from 0.3 to 0.05 keV. Since the final slice energy spread is expected to be on the 1 keV level, such an error reduction is very important.

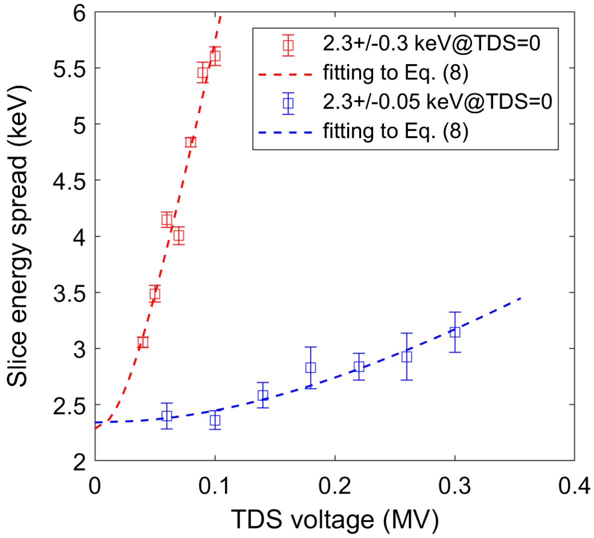

FIG. 9. Slice energy spread versus TDS voltage. Red curve is measured without slit 1 cut, and blue curve is measured with vertical emittance cut by slit 1.

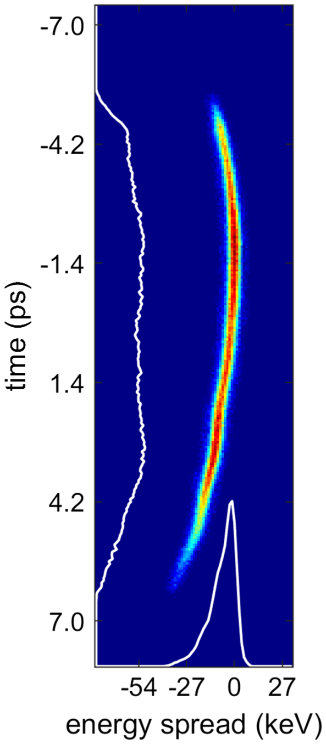

FIG. 10. Longitudinal phase space at 140 kV TDS voltage with two slits inserted, and the bunch charge is reduced from 250 to 5 pC.

As discussed in Sec. II C, when 50 μm slit 2 vertical slit is inserted, the emittance-induced horizontal rms size on Disp3.scr1 approximates $R_{12x,\mathrm{D3}} \cdot \sigma_{x'\mathrm{slit2}}$. The beam divergence after slit 2 is measured at High2.scr2 when the dipole magnet is off. In order to remove the screen resolution contribution, quadrupole group 3 is used to vary $R_{12x,\mathrm{H2}}$, and both the screen resolution and beam divergence can be fitted based on Eq. (12). Here, the beam rms size σ_x at

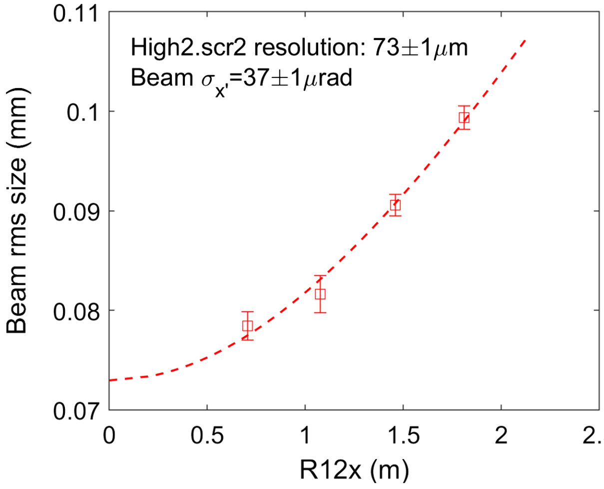

FIG. 11. Screen resolution and beam divergence measurements at High2.scr2.

High2.scr2 is measured for the same time slice as that used for slice energy spread calculation. The measurement results are displayed in Fig. 11, which gives a slice beam divergence of 37 ± 1 μrad. Based on the 50 μm slit width and the slice beam divergence, a normalized horizontal slice emittance of 20 nm can be evaluated. $R_{12x,\mathrm{D3}}$ is measured by orbital response to be 0.81 m, so the emittance-induced beam size on the dispersion screen can be calculated with the product of slice beam divergence after the second slit and $R_{12x,\mathrm{D3}}$ to be 30 ± 1 μm. Based on the dispersion of 0.9 m and beam momentum of 19.5 MeV/c, the slice emittance contributes to an energy spread resolution of 0.65 ± 0.02 keV.

The screen resolution of Disp3.scr1 is measured at the nondispersion direction when TDS is off, so vertical slit 2 is changed to horizontal slit 2. The measurement is based on Eq. (11), and R_{12y} is varied by quadrupole group 3. The screen resolution is 69 ± 1 μm as shown in Fig. 12, and this translates to an energy spread resolution of 1.50 ± 0.02 keV based on Eq. (5). In order to increase the signal to noise ratio of the streaked 5 pC beam at Disp3.scr1, 2 × 2 pixel binning was used, and the image calibration is 62.8 μm/pixel. The screen resolution in the nonbinning mode is measured to be 53 ± 4 μm, which shows the screen resolution in the binning mode is not due to the material itself.

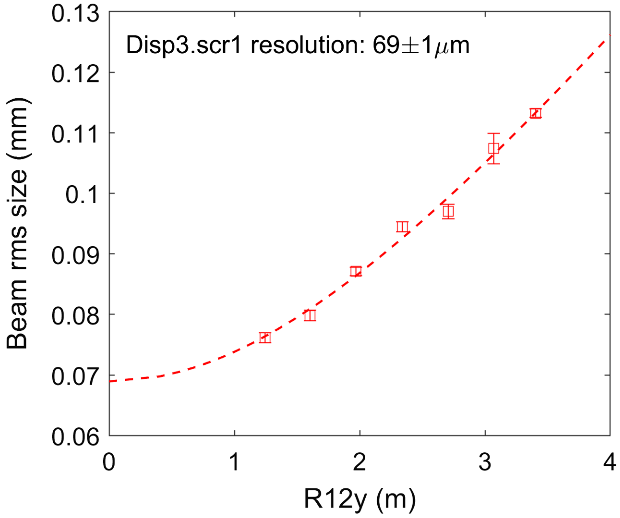

FIG. 12. Screen resolution measurements at Disp3.scr1.

TABLE III. Summary of the slice energy spread measurement decompositions for the 5-pC beam collimated from the 250-pC beam, both in beam size measured at Disp3.scr1 and in energy spread.

Non-TDS contribution	Screen resolution	Emittance resolution	Real slice energy spread	Units
107 ± 2	69 ± 1	30 ± 1	76 ± 2	μm
2.32 ± 0.05	1.50 ± 0.02	0.65 ± 0.02	1.65 ± 0.06	keV

With both screen resolution and emittance contribution measured, the slice energy spread decomposition is summarized in Table III. The slice energy spread is 1.65 ± 0.06 keV for the ~5 pC beam, which is from two slit cuts of the 250 pC beam. Based on the simulations in Fig. 7, it indicates the full beam slice energy spread is 2.07 ± 0.05 keV, and additional uncorrelated heating of 1.52 ± 0.06 keV is needed to add to the start-to-end simulations to explain the measurements.

IV. DISCUSSIONS

For the 250 pC working point, two slits were used to cut the beam transverse emittance for improving LPS measurement resolutions, and the bunch charge is reduced from 250 to 5 pC after two slits, for which 1.65 ± 0.06 keV slice energy spread was measured. Start-to-end simulations of the measurement only give a slice energy spread of 0.75 keV rms after the two slit cuts as shown in Fig. 7. In order to fit the experiment results, an additional uncorrelated slice energy spread of 1.52 keV is added to the beam at the first slit entrance, leading to a full beam slice energy spread of 2.07 keV at the first slit entrance. This is almost a factor of 3 lower than that measured at high energy (130 MeV) photoinjector at European XFEL. Both injectors operate with similar gun parameters, similar laser distributions and same cathodes, and have the same peak current of 20 A. Our result demonstrates the expected low slice energy spread (~2 keV) from the Cs_2Te based photoinjector and indicates slice energy spread growth in the high energy photoinjector, e.g., intrabeam scattering, microbunching instability, which is worth further studies.

V. SUMMARY

Longitudinal phase space mapping by TDS and dipole magnet is used for direct slice energy spread measurement, but its energy resolution is limited by screen resolution, emittance-induced beam size, and TDS-induced energy spread. Analytical analysis shows a low energy beam can achieve better energy resolution than a high energy beam with the same normalized emittance, beta function, dispersion function, and screen resolution. The product of time and energy resolution of TDS streaking is limited by the beam emittance. Therefore, we used a beam of lower energy and reduced horizontal and vertical emittance by slit cutting to enhance the LPS resolutions.

Numerical simulations show the lowest TDS-induced energy spread during a TDS voltage scan should be as small as possible to minimize the fitting uncertainty of non-TDS related energy spread. Besides, the time resolution at the lowest TDS voltage should be good as well, otherwise energy curvature combined with limited time resolution will lead to slice energy spread measurement errors. Direct measurements of energy spread resolutions due to screen resolution and emittance-induced beam size were suggested and demonstrated by using slit and lattice scans, which does not require a constant beta function like previous methods used for high energy injectors [31,32]. Start-to-end simulations show the method can measure the true screen resolution and slice emittance contributions at the dispersion screen. Simulations also show the reconstructed energy spread is only valid for the beam after the slits. This is due to a correlation between the slice energy distribution and the transverse coordinates of the space-charge dominated beam before the slits. For special cases in which the above correlation is negligible, the reconstructed energy spread after the slits can also be close to that of the full beam before the slits.

Finally, we demonstrated the new methods by measuring the slice energy spread at PITZ, which mimic the best emittance working point for European XFEL at 20 MeV. After two slit cuts of the 250 pC beam, the bunch charge is 5 pC and the measured slice energy spread is 1.65 ± 0.06 keV. According to our simulations, this corresponds to an energy spread for the full beam of 2.07 keV at the first slit entrance. This value indicates a significant heating effect of 1.52 keV not included in the modeling. Compared to the high energy (≥ 100 MeV) injector results from SwissFEL and European XFEL, this indicates significant slice energy spread growth in the high energy injector.

ACKNOWLEDGMENTS

The authors appreciate discussions with S. Tomin, I. Zagorodnov, E. Gjonaj, T. Limberg, and the other colleagues of the European XFEL beam dynamics team. This work was supported by the European XFEL research and development program.

[1] D. B. Williams and C. B. Carter, The transmission electron microscope, in *Transmission Electron Microscopy* (Springer, New York, 1996), pp. 3–17.

[2] C. Pellegrini, X-ray free-electron lasers: From dreams to reality, Phys. Scr. **2016**, 014004 (2017).

[3] C. Bostedt, S. Boutet, D. M. Fritz, Z. Huang, H. J. Lee, H. T. Lemke, A. Robert, W. F. Schlotter, J. J. Turner, and G. J. Williams, Linac coherent light source: The first five years, Rev. Mod. Phys. **88**, 015007 (2016).

[4] J. Rossbach, J. R. Schneider, and W. Wurth, 10 years of pioneering x-ray science at the free-electron laser flash at DESY, Phys. Rep. **808**, 1 (2019).

[5] Z. Huang and K.-J. Kim, Review of x-ray free-electron laser theory, Phys. Rev. ST Accel. Beams **10**, 034801 (2007).

[6] J. Rosenzweig, N. Majernik, R. Robles, G. Andonian, O. Camacho, A. Fukasawa, A. Kogar, G. Lawler, J. Miao, P. Musumeci *et al.*, An ultra-compact x-ray free-electron laser, New J. Phys. **22**, 093067 (2020).

[7] M. Huning and H. Schlarb, Measurement of the beam energy spread in the TTF photo-injector, in *Proceedings of the 2003 Particle Accelerator Conference, Portland, OR* (IEEE, New York, 2003), Vol. 3, pp. 2074–2076.

[8] E. Saldin, E. Schneidmiller, and M. Yurkov, Klystron instability of a relativistic electron beam in a bunch compressor, Nucl. Instrum. Methods Phys. Res., Sect. A **490**, 1 (2002).

[9] Z. Huang and K.-J. Kim, Formulas for coherent synchrotron radiation microbunching in a bunch compressor chicane, Phys. Rev. ST Accel. Beams**5**, 074401 (2002).

[10] D. Ratner, C. Behrens, Y. Ding, Z. Huang, A. Marinelli, T. Maxwell, and F. Zhou, Time-resolved imaging of the microbunching instability and energy spread at the linac coherent light source, Phys. Rev. ST Accel. Beams **18**, 030704 (2015).

[11] J. Qiang, Y. Ding, P. Emma, Z. Huang, D. Ratner, T. Raubenheimer, M. Venturini, and F. Zhou, Start-to-end simulation of the shot-noise driven microbunching instability experiment at the linac coherent light source, Phys. Rev. Accel. Beams **20**, 054402 (2017).

[12] S. Heifets, G. Stupakov, and S. Krinsky, Coherent synchrotron radiation instability in a bunch compressor, Phys. Rev. ST Accel. Beams **5**, 064401 (2002).

[13] Z. Huang, A. Brachmann, F.-J. Decker, Y. Ding, D. Dowell, P. Emma, J. Frisch, S. Gilevich, G. Hays, P. Hering *et al.*, Measurements of the linac coherent light source laser heater and its impact on the x-ray free-electron laser performance, Phys. Rev. ST Accel. Beams **13**, 020703 (2010).

[14] S. Spampinati, E. Allaria, L. Badano, S. Bassanese, S. Biedron, D. Castronovo, P. Craievich, M. Danailov, A. Demidovich, G. De Ninno *et al.*, Laser heater commissioning at an externally seeded free-electron laser, Phys. Rev. ST Accel. Beams **17**, 120705 (2014).

[15] J. Lee, J.-H. Han, S. Lee, J. Hong, C. H. Kim, C. K. Min, and I. S. Ko, PAL-XFEL laser heater commissioning, Nucl. Instrum. Methods Phys. Res., Sect. A **843**, 39 (2017).

[16] T. Ishikawa, H. Aoyagi, T. Asaka, Y. Asano, N. Azumi, T. Bizen, H. Ego, K. Fukami, T. Fukui, Y. Furukawa *et al.*, A compact x-ray free-electron laser emitting in the sub-ångström region, Nat. Photonics **6**, 540 (2012).

[17] E. Prat, R. Abela, M. Aiba, A. Alarcon, J. Alex, Y. Arbelo, C. Arrell, V. Arsov, C. Bacellar, C. Beard *et al.*, A compact and cost-effective hard x-ray free-electron laser driven by a high-brightness and low-energy electron beam, Nat. Photonics **14**, 748 (2020).

[18] G. D'Auria *et al.*, The CompactLight Design Study Project, in *Proceedings of the 10th International Particle Accelerator Conference, IPAC-2019, Melbourne, Australia, 2019* (JACoW Publishing, Geneva, Switzerland, 2019), pp. 1756–1759, 10.18429/JACoW-IPAC2019-TUPRB032.

[19] J. N. Galayda *et al.*, The LINAC Coherent Light Source-II Project, in *Proceedings of the 5th International Particle Accelerator Conference, IPAC-2014, Dresden, Germany* (JACoW, Geneva, Switzerland, 2014), p. 935.

[20] R. Brinkmann, E. Schneidmiller, J. Sekutowicz, and M. Yurkov, Prospects for CW and LP operation of the European XFEL in hard x-ray regime, Nucl. Instrum. Methods Phys. Res., Sect. A **768**, 20 (2014).

[21] B. W. Zhao, Zhentang Zhao: Past and future of the Shanghai Synchrotron Radiation Facility, National political science review **8**, nwab185 (2021).

[22] I. V. Bazarov, B. M. Dunham, and C. K. Sinclair, Maximum Achievable Beam Brightness from Photoinjectors, Phys. Rev. Lett. **102**, 104801 (2009).

[23] C. Limborg-Deprey, C. Adolphsen, D. McCormick, M. Dunning, K. Jobe, H. Li, T. Raubenheimer, A. Vrielink, T. Vecchione, F. Wang *et al.*, Performance of a first generation x-band photoelectron rf gun, Phys. Rev. Accel. Beams **19**, 053401 (2016).

[24] D. Alesini, G. Castorina, M. Croia, M. Ferrario, A. Gallo, B. Spataro, C. Vaccarezza, and A. Vannozzi, Design of a full c-band injector for ultra-high brightness electron beam, in *Proceedings of the 10th International Particle Accelerator Conference, IPAC-2019, Melbourne, Australia, 2019* (JACoW, Geneva, Switzerland, 2019).

[25] M. Schaer, A. Citterio, P. Craievich, L. Stingelin, R. Zennaro *et al.*, Study of a C-band TW electron gun for SwissFEL, in *Proceedings of the 5th International Particle Accelerator Conference, IPAC-2014, Dresden, Germany* (JACoW, Geneva, Switzerland, 2014).

[26] L. Wang, W. Fang, J. Tan, X. Huang, W. Zhang, C. Wang, and Z. Zhao, Design, fabrication and cold-test results of a 3.6 cell C-band photocathode rf gun for SXFEL, Nucl. Instrum. Methods Phys. Res., Sect. A **1003**, 165320 (2021).

[27] D. Filippetto, P. Musumeci, M. Zolotorev, and G. Stupakov, Maximum current density and beam brightness achievable by laser-driven electron sources, Phys. Rev. ST Accel. Beams **17**, 024201 (2014).

[28] C. Gulliford, A. Bartnik, I. Bazarov, B. Dunham, and L. Cultrera, Demonstration of cathode emittance dominated high bunch charge beams in a dc gun-based photoinjector, Appl. Phys. Lett. **106**, 094101 (2015).

[29] F. Sannibale, D. Filippetto, H. Qian, C. Mitchell, F. Zhou, T. Vecchione, R. Li, S. Gierman, and J. Schmerge, High-brightness beam tests of the very high frequency gun at the advanced photo-injector experiment test facility at the Lawrence Berkeley National Laboratory, Rev. Sci. Instrum. **90**, 033304 (2019).

[30] H. Qian, E. Vogel *et al.*, Overview of CW rf guns for short wavelength FELs, in *Proceedings of the 39th Free Electron Laser Conference (FEL'19), Hamburg, Germany, 2019* (JACoW Publishing, Geneva, Switzerland, 2019), pp. 290–296, 10.18429/JACoW-FEL2019-WEA01.

[31] E. Prat, P. Dijkstal, E. Ferrari, A. Malyzhenkov, and S. Reiche, High-resolution dispersion-based measurement of the electron beam energy spread, Phys. Rev. Accel. Beams **23**, 090701 (2020).

[32] S. Tomin, I. Zagorodnov, W. Decking, N. Golubeva, and M. Scholz, Accurate measurement of uncorrelated energy spread in electron beam, Phys. Rev. Accel. Beams **24**, 064201 (2021).

[33] C. Feng, T. Zhang, J. Chen, H. Deng, M. Zhang, X. Wang, B. Liu, T. Lan, D. Wang, and Z. Zhao, Measurement of the average local energy spread of electron beam via coherent harmonic generation, Phys. Rev. ST Accel. Beams **14**, 090701 (2011).

[34] G. Penco, E. Allaria, G. De Ninno, E. Ferrari, and L. Giannessi, Experimental Demonstration of Enhanced Self-Amplified Spontaneous Emission by an Optical Klystron, Phys. Rev. Lett. **114**, 013901 (2015).

[35] E. Prat, E. Ferrari, M. Calvi, R. Ganter, S. Reiche, and T. Schmidt, Demonstration of a compact x-ray free-electron laser using the optical klystron effect, Appl. Phys. Lett. **119**, 151102 (2021).

[36] L.-H. Yu, L. DiMauro, A. Doyuran, W. Graves, E. Johnson, R. Heese, S. Krinsky, H. Loos, J. Murphy, G. Rakowsky *et al.*, First Ultraviolet High-Gain Harmonic-Generation Free-Electron Laser, Phys. Rev. Lett. **91**, 074801 (2003).

[37] G. Stupakov, Using the Beam-Echo Effect for Generation of Short-Wavelength Radiation, Phys. Rev. Lett. **102**, 074801 (2009).

[38] E. Allaria, D. Castronovo, P. Cinquegrana, P. Craievich, M. Dal Forno, M. Danailov, G. D'Auria, A. Demidovich, G. De Ninno, S. Di Mitri *et al.*, Two-stage seeded soft-x-ray free-electron laser, Nat. Photonics **7**, 913 (2013).

[39] P. Rebernik Ribič, A. Abrami, L. Badano, M. Bossi, H.-H. Braun, N. Bruchon, F. Capotondi, D. Castronovo, M. Cautero, P. Cinquegrana *et al.*, Coherent soft x-ray pulses from an echo-enabled harmonic generation free-electron laser, Nat. Photonics **13**, 555 (2019).

[40] G. Penco, G. Perosa, E. Allaria, S. Di Mitri, E. Ferrari, L. Giannessi, S. Spampinati, C. Spezzani, and M. Veronese, Enhanced seeded free electron laser performance with a "cold" electron beam, Phys. Rev. Accel. Beams **23**, 120704 (2020).

[41] Z. Huang, A. Brachmann, F.-J. Decker, Y. Ding, D. Dowell, P. Emma, J. Frisch, S. Gilevich, G. Hays, P. Hering, R. Iverson, H. Loos, A. Miahnahri, H.-D. Nuhn, D. Ratner, G. Stupakov, J. Turner, J. Welch, W. White, J. Wu, and D. Xiang, Measurements of the linac coherent light source laser heater and its impact on the x-ray free-electron laser performance, Phys. Rev. ST Accel. Beams **13**, 020703 (2010).

[42] D. Marx, R. Assmann, P. Craievich, U. Dorda, A. Grudiev, and B. Marchetti, Longitudinal phase space reconstruction simulation studies using a novel x-band transverse deflecting structure at the SINBAD facility at DESY, Nucl. Instrum. Methods Phys. Res., Sect. A **909**, 374 (2018).

[43] K. Floettmann and V. V. Paramonov, Beam dynamics in transverse deflecting rf structures, Phys. Rev. ST Accel. Beams **17**, 024001 (2014).

[44] M. Scholz, Beam optics and emittance measurement evaluations 2019 and 2020, XFEL Beam dynamics meeting, https://www.desy.de/fel-beam/s2e/talks/2020_12_15/matthias.pdf (2020).

[45] D. Malyutin, Time resolved transverse and longitudinal phase space measurements at the high brightness photo injector PITZ, Ph.D. thesis, University of Hamburg, Hamburg, 2014.

[46] D. Malyutin, M. Krasilnikov, M. Otevrel, and F. Stephan, Simulation of the longitudinal phase space measurements with the transverse deflecting structure at PITZ, in *Proceedings of the 3rd International Particle Accelerator Conference IPAC2012, New Orleans, LA* (JACoW, Geneva, Switzerland, 2012), MOPPP034.

[47] H. Huck, P. Boonpornprasert, L. Jachmann, W. Koehler, M. Krasilnikov, A. Oppelt, F. Stephan *et al.*, Progress on the PITZ TDS, in *Proceedings of of the 5th International Beam Instrumentation Conference, Barcelona, Spain* (JACoW, Geneva, Switzerland, 2016), pp. 744–747.

[48] B. Dwersteg, K. Flöttmann, J. Sekutowicz, and C. Stolzenburg, rf gun design for the TESLA VUV Free Electron Laser, Nucl. Instrum. Methods Phys. Res., Sect. A **393**, 93 (1997).

[49] F. Stephan, C. Boulware, M. Krasilnikov, J. Bähr, G. Asova, A. Donat, U. Gensch, H. Grabosch, M. Hänel, L. Hakobyan *et al.*, Detailed characterization of electron sources yielding first demonstration of European x-ray free-electron laser beam quality, Phys. Rev. ST Accel. Beams **13**, 020704 (2010).

[50] M. Krasilnikov, F. Stephan, G. Asova, H.-J. Grabosch, M. Groß, L. Hakobyan, I. Isaev, Y. Ivanisenko, L. Jachmann, M. Khojoyan *et al.*, Experimentally minimized beam emittance from an l-band photoinjector, Phys. Rev. ST Accel. Beams **15**, 100701 (2012).

[51] L. Staykov and I. Tsakov, Design optimization of an emittance measurement system at PITZ, in *Proceedings of the 7th European Workshop on Beam Diagnostics and Instrumentation for Particle Accelerators, Lyon, France, 2005* (2005), https://accelconf.web.cern.ch/d05/.

[52] S. Huang, Intrabeam scattering in an x-ray FEL driver, SLAC National Accelerator Laboratory, Menlo Park, CA, Technical Report No. SLAC-TN-05-026, 2018.

[53] S. Di Mitri, G. Perosa, A. Brynes, I. Setija, S. Spampinati, P. Williams, A. Wolski, E. Allaria, S. Brussaard, L. Giannessi *et al.*, Experimental evidence of intrabeam scattering in a free-electron laser driver, New J. Phys. **22**, 083053 (2020).

[54] K. Floettmann, ASTRA: A space charge tracking algorithm, https://www.desy.de/%7empyflo/.

[55] S. Tomin, I. Agapov, M. Dohlus, and I. Zagorodnov, OCELOT as a framework for Beam Dynamics Simulations of x-ray sources, in *Proceedings of the 8th International Particle Accelerator Conference, IPAC-2017, Copenhagen, Denmark* (JACoW, Geneva, Switzerland, 2017).

[56] E. Gjonaj, in *Proceedings of the 2022 Free Electron Laser Conference* (2022).

[57] Y. Chen, I. Zagorodnov, and M. Dohlus, Beam dynamics of realistic bunches at the injector section of the European x-ray free-electron laser, Phys. Rev. Accel. Beams **23**, 044201 (2020).

[58] M. Gross, N. Aftab, P. Boonpornprasert, Y. Chen, G. Georgiev, J. Good, C. Koschitzki, M. Krasilnikov, X. Li, O. Lishilin, G. Loisch, D. Melkumyan, S. Mohanty, R. Niemczyk, A. Oppelt, H. Qian, G. Shu, F. Stephan, G. Vashchenko, and I. Will, Characterization of low emittance electron beams generated by transverse laser beam shaping, in *Proceedings of the 12th International Particle Accelerator Conference, IPAC-2021, Campinas, SP, Brazil* (JACoW Publishing, Geneva, Switzerland, 2021), pp. 2690–2692, 10.18429/JACoW-IPAC2021-WEPAB040.

[59] C. Wiebers, M. Holz, G. Kube, D. Noelle, G. Priebe, and H.-C. Schröder, Scintillating screen monitors for transverse electron beam profile diagnostics at the European XFEL, in *Proceedings of the 2nd Beam Instrumentation Conference, IBIC-2013, Oxford, UK* (JACoW, Geneva, Switzerland, 2013).